Normally-off boron-doped diamond MOSFETs with a breakdown voltage over 1.7 kV

J. Liu,[1, a)] T. Teraji,[1] B. Da,[2] and Y. Koide[1, b)]

[1]*Research Center for Electronic and Optical Materials, National Institute for Materials Science (NIMS), 1-1 Namiki, Tsukuba, Ibaraki 305-0044, Japan*

[2]*Research and Services Division of Materials Data and Integrated System, NIMS, 1-1 Namiki, Tsukuba, Ibaraki 305-0044, Japan*

[a)] Author to whom correspondence should be addressed; electronic mail: liu.jiangwei@nims.go.jp

[b)] The present affiliation is School of Science and Technology, Mejyo University.

Abstract

Boron-doped diamond (B-diamond) metal-oxide-semiconductor field-effect transistors (MOSFETs) are fabricated on a 150 nm-thick epitaxial layer. The threshold voltage of the B-diamond MOSFET is measured at -8.0 V, indicating a normally-off behavior. Due to the high activation energy for the boron dopants and the relatively thin epitaxial layer, a limited number of holes are formed in the B-diamond and potentially trapped within the Al_2O_3/B-diamond interface, leading to the normally-off behavior observed in the B-diamond MOSFET. The absolute breakdown voltage for the B-diamond MOSFET is found to exceed 1.7 kV. When divided by the gate-to-drain electrode length of 11.3 μm, the breakdown field is calculated to be 1.52 MV/cm, which is more than two times larger than that of the previous B-diamond MOSFETs.

Diamond, a wide-bandgap semiconductor, exhibits exceptional intrinsic properties in contrast to other semiconductors.[1,2] These properties include a high critical breakdown field, large thermal conductivity, high carrier mobility, chemical inertness, and radiation hardness. Diamond-based electronic devices show great promise due to their efficient operation with minimal power loss, high power-frequency capabilities, impressive thermal management, and stable performance in harsh radiation environments.

Recently, significant progress has been achieved in the development of *p*-type hydrogen-terminated diamond (H-diamond)[3-8] and boron-doped diamond (B-diamond)[9-13] based metal-oxide-semiconductor field-effect transistors (MOSFETs). In the H-diamond channel layer, two-dimensional hole gases form on its surface. While the exact mechanism of this formation is still a topic of debate, two conditions of the presence of surface carbon-hydrogen bonds and negatively charged acceptors are essential.[14, 15] These negatively charged acceptors possess the capability to trap electrons from the H-diamond, leading to the creation of hole gases on the H-diamond surface. However, the surface hole gases are not stable at high-temperatures, possibly due to the damage of the negative charge acceptors. The electrical characteristics of H-diamond MOSFETs exhibited a significant degradation as the annealing temperature surpasses 300°C.[16]

On the other hand, the B-diamond-based MOSFETs are known to perform well at high-temperatures. In recent research, we employed a relatively flat B-diamond epitaxial layer integrated with a large-area Ohmic contact to create high-performance B-diamond MOSFETs.[13, 17] The flat B-diamond surface aids in reducing carrier surface scattering and improving the quality of the gate oxide/B-diamond interface. The large-area Ohmic contact helps in lowering the on-resistance and increasing the output

current of the B-diamond MOSFETs.

The maximum drain current ($I_{D,max}$) of the B-diamond MOSFETs operating at room temperature and 300°C has been significantly enhanced to -1.2 and -10.9 mA/mm, respectively.[17] However, a notable challenge for the B-diamond MOSFETs remains their high threshold voltage (V_{TH}) values, which are recorded at 63.8 V and 31.2 V at room temperature and 300°C, respectively. Previous research has shown that reducing the thickness of the channel layer can substantially decrease V_{TH} for B-diamond MOSFETs.[18] In the case of a similar boron doping level, we observed that by reducing the epitaxial layer thickness from 2650 nm to 800 nm, the V_{TH} values for B-diamond MOSFETs could be lowered to below 3.4 V, with the lowest threshold voltage being 0.8 V.[18]

In this study, we have reduced the epitaxial layer thickness to approximately 150 nm to investigate the V_{TH} for the B-diamond MOSFET. Our findings reveal that the V_{TH} for the B-diamond MOSFET is measured at -8.0 V, indicating a normally-off behavior. We have also examined the breakdown voltages of the B-diamond MOSFETs at a gate-to-source voltage (V_{GS}) of 0 V.

A B-diamond epitaxial layer was grown on an Ib-type (100) diamond substrate using microwave plasma-assisted chemical vapor deposition under the following conditions: microwave power of 1.4 kW, temperature maintained around ~1000 °C, and chamber pressure set at 18.6 kPa.[19] The flow rates for the source gases of H_2 and CH_4 were 49 and 1 sccm, respectively. Boron doping was achieved utilizing residual boron present in the chamber from the previous B-diamond growth. The concentration profile of boron atoms in the B-diamond epitaxial layer was analyzed through depth profiling of a secondary ion mass spectrometry (SIMS) technique, as illustrated in Fig. 1(a). The

thickness of the boron-doped diamond epitaxial layer is approximately 150 nm, with boron concentrations ranging between 10^{16} to 10^{17} cm^{-3}.

The B-diamond epitaxial layer underwent treatment at 300 °C for 3 hours in a mixed solution of H_2SO_4 and HNO_3 to alter its hydrogen-terminated surface to oxygen-terminated. Subsequently, the B-diamond was coated sequentially with a positive photoresist LOR5A followed by an image reversal photoresist AZ5214E using a spin-coater. The spin speed and time for coating both photoresists were set at 7000 rpm and 1 second, respectively. Baking parameters for LOR5A were a temperature of 180 °C and a duration of 5 minutes, while for AZ5214E, the temperature and time were 110 °C and 2 minutes, respectively. The exposure and development processes were carried out using a DL-1000 scanning maskless lithography system and tetramethylammonium hydroxide solution with a concentration of 2.38%, respectively. The developing process in the TMAH solution took approximately 2.0 minutes.

The source/drain electrodes, composed of a Ti/Au bilayer (10/150 nm), were deposited on the B-diamond using an electron-gun evaporation system. The chamber pressure during the evaporation of the Ti/Au bilayer was maintained at approximately 10^{-6} Pa, with evaporation rates set at 1 Å/s for Ti and 2 Å/s for Au. Subsequently, the electrodes underwent annealing at 550 °C for 20 minutes in an Ar atmosphere using a rapid thermal annealing system to establish Ohmic contacts. An Al_2O_3 gate oxide layer was then deposited via atomic layer deposition technique at 250 °C utilizing $Al(CH_3)_3$ and ozone precursors. For the gate electrode, a Ti/Au bilayer (10/150 nm) was employed. A cross-sectional high-resolution transmission electron microscope (TEM) image of the Al_2O_3/B-diamond interface is presented in Fig. 1 (b), revealing an abrupt interface. The thickness of the Al_2O_3 film was measured to be 21.2 nm.

To access the source/drain electrodes, windows were opened by etching the Al_2O_3 film using a capacitively coupled plasma reactive-ion etching system in a CHF_3 + Ar atmosphere. The etching process involved a plasma power of 100 W, chamber pressure of 3.0 Pa, CHF_3 flow rate of 10 sccm, and Ar flow rate of 40 sccm. The electrical properties of the B-diamond MOSFETs were characterized using a Grail 10-5-LV-HTV prober system.

Figures 2(a) and 2(b) shows a scanning electron microscopy image and schematic diagram of the B-diamond MOSFET, respectively. The diameter for the drain electrode is 398.2 μm. The gate width can be calculated as 1250.3 μm. The gate length is 3.0 μm. The interspatial lengths for the gate-to-source and gate-to-drain electrodes ($L_{G\text{-}S}$ and $L_{G\text{-}D}$) are 5.0 and 11.3 μm, respectively.

Figure 3(a) depicts the I_D as a function of drain voltage (V_D) for the B-diamond MOSFET. The V_{GS} ranges from -16.0 to 40.0 V in increments of +1.0 V, showcasing distinct saturation regions and *p*-type characteristics. The absolute $I_{D,max}$ for the B-diamond MOSFET is 0.12 μA/mm, significantly lower than the maximum value of 1.2 mA/mm reported previously.[11, 17] This difference could be attributed to the much thinner epitaxial layer thickness (from 2650 nm to 150 nm), the increased L_G, and the larger $L_{G\text{-}D}$. The on/off ratio for the B-diamond MOSFET was determined to be greater than 10^4. The off-current is below 10^{-6} μA/mm, consistent with the previous report.[17] However, due to the low on-current observed in the current MOSFET, its on/off ratio is notably lower than the previous report of 10^9. [17]

Figure 4(a) illustrates the $-\sqrt{|I_D|}$–V_{GS} characteristic for the B-diamond MOSFET. The V_{TH} is determined to be -8.0 V, indicating a normally-off behavior. This marks the first demonstration of a normally-off *p*-type B-diamond MOSFET. There are several reports

for the normally-off *p*-type H-diamond or silicon-terminated diamond (Si-diamond) based MOSFETs.[20-26] The formation of normally-off characteristics for the H-diamond and Si-diamond MOSFETs can be achieved by modifying the two necessary conditions of carbon-hydrogen bonds and negatively charged acceptors for the channel layers. As the carbon-hydrogen bonds damaged by surface etching changing to carbon-oxygen bonds partially[24-26] and the negatively charges acceptorts compensated by positive charges in the oxide insulators,[21-23] the hole gases in the H-diamond and Si-diamond channel layers cannot formed. These are the formation mechanism for the normally-off behaviors of the H-diamond and Si-diamond MOSFETs. On the other hand, a selective growth of a *p*-type epitaxial layer on the *n*-type diamond body with hydroxy-termination can also lead to the formation of normally-off characteristics for the diamond MOSFETs.[27, 28]

On the other hand, previous reports on the *p*-type B-diamond MOSFETs all exhibited normally-on behaviors.[9-13, 17] In this study, we have successfully developed a normally-off B-diamond MOSFET by reducing the epitaxial thickness. The inset figure in Fig. 4(a) illustrates the schematic diagram depicting the formation mechanism of the normally-off characteristic of the B-diamond MOSFET. Due to the high activation energy required for boron dopants and the thin epitaxial layer thickness, only a limited number of holes are generated in the B-diamond. Furthermore, the presence of defects and oxygen vacancies at the Al_2O_3/B-diamond interface facilitates the potential capture of these limited holes within the interface, providing an explanation for the normally-off behavior of the B-diamond MOSFET.

The breakdown voltage (V_B) values for two B-diamond MOSFETs were measured and are depicted in Fig. 4(b) as -1612 and -1718 V, respectively. Dividing these values

by the $L_{G\text{-}D}$ (11.3 μm) yields breakdown fields of 1.43 and 1.52 MV/cm, respectively. These values are more than two times larger than the 0.67 MV/cm of the previous reported B-diamond MOSFET with $V_B/L_{G\text{-}D}$ of 200 V/3.0 μm.[29] Furthermore, they are better than the breakdown fields of other devices, including the B-diamond metal-semicondutor FET of 1.39 and 0.51 MV/cm with the $V_B/L_{G\text{-}D}$ values of 693 V/5.0 μm and 1530 V/30 μm, [30] and the H-diamond MOSFET of 0.73 MV/cm with the $V_B/L_{G\text{-}D}$ of 3659 V/50 μm.[31]

In this study, the B-diamond MOSFETs were fabricated on a 150 nm-thick thin epitaxial layer. The V_{TH} of the B-diamond MOSFET was recorded at -8.0 V, indicating the normally-off behavior. The limited holes in the thin B-diamond epitaxial layer were formed and captured within the Al_2O_3/B-diamond interface potentially, explaining the normally-off behavior. The absolute V_B and electrical field for the B-diamond MOSFET were measured to be 1718 V and 1.52 MV/cm, respectively.

This work is supported by the JSPS KAKENHI Projects (JP23K03966, 20H05661, and JP20H00313), MEXT Q-LEAP (JPMXS0118068379), JST CREST (JPMJCR1773), JST Moonshot R&D (JPMJMS2062), MIC R&D for construction of a global quantum cryptography network (JPMI00316), and ARIM (23WS0311 and 23NM5006) of the Ministry of Education, Culture, Sports, Science and Technology, Japan.

Data Availability Statements

The data that support the findings of this study are available from the corresponding author upon reasonable request.

References

1. C. J. H. Wort and R. S. Balmer, Mater. Today **11**, 22 (2008).
2. H. Umezawa, Mater. Sci. Semi. Proc. **78**, 147 (2018).
3. K. Hirama, H. Sato, Y. Harada, H. Yamamoto, and M. Kasu, Jpn. J. Appl. Phys. **51**, 090112 (2012).
4. J. Liu, H. Ohsato, M. Y. Liao, M. Imura, E. Watanabe, and Y. Koide, IEEE Electron Dev. Lett. **38**, 922–925 (2017).
5. Z. Ren, J. Zhang, J. Zhang, C. Zhang, S. Xu, Y. Li, and Y. Hao, IEEE Electron Dev. Lett. **38**, 786–789 (2017).
6. W. Wang, Y. Wang, M. Zhang, R. Wang, G. Chen, X. Chang, F. Lin, F. Wen, K. Jia, and H. X. Wang, IEEE Electron Dev. Lett. **41**, 585 (2020).
7. W. Fei, T. Bi, M. Iwataki, S. Imanishi, and H. Kawarada, Appl. Phys. Lett. **116**, 212103 (2020).
8. X. Yu, J. Zhou, C. Qi, Z. Cao, Y. Kong, and T. Chen, IEEE Electron Dev. Lett. **39**, 1373–1376 (2019).
9. T. T. Pham, J. Pernot, G. Perez, D. Eon, E. Gheeraert, and N. Rouger, IEEE Electron Dev. Lett. **38**, 1571–1574 (2017).
10. T. T. Pham, M. Gutiérrez, C. Masante, N. Rouger, D. Eon, E. Gheeraert, D. Araùjo, and J. Pernot, Appl. Phys. Lett. **112**, 102103 (2018).
11. Z. Zhu, Z. Ren, Y. Li, J. Zhang, K. Su, L. Zhu, J. Meng, J. Chen, and Y. Hao, IEEE Electron Dev. Lett. **45**, 1694-1697 (2024).
12. J. Liu, T. Teraji, B. Da and Y. Koide, IEEE Tran. Electron Dev. **68**, 3963–3967 (2021).

13. J. Liu, T. Teraji, B. Da and Y. Koide, IEEE Tran. Electron Dev. **70**, 2199–2203, (2023).
14. D. Takeuchi, M. Riedel, J. Risterin, and L. Ley, Phys. Rev. B **68**, 041304 (2003).
15. C. I. Pakes, J. A. Garrido, and H. Kawarada, MRS Bulletin **39**, 542 (2014).
16. J. Liu, H. Oosato, B. Da, T. Teraji, A. Kobayashi, H. Fujioka, and Y. Koide, J. Phys. D: Appl. Phys. **52**, 315104 (2019).
17. J. Liu, T. Teraji, B. Da and Y. Koide, Appl. Phys. Lett. **124**, 072103 (2024).
18. J. Liu, T. Teraji, B. Da and Y. Koide. IEEE Tran. Electron Dev. **71,** 1764-1768 (2024).
19. T. Teraji, T. Yamamoto, K. Watanabe, Y. Koide, J. Isoya, S. Onoda, T. Ohshima, L. J. Rogers, F. Jelezko, P. Neumann, J. Wrachtrup, and S. Koizumi, Physica Status Solidi A **212**, 2365–2384 (2015).
20. M. Li, X. Zhang, S. Jiao, Y. Wang, S. Wei, J. Yan, J. Zhang, and X. Zhang, Recent advances in diamond MOSFETs with normally off characteristics. Funct. Dia. **4** 2357654 (2024).
21. J. Liu, M. Liao, M. Imura, and Y. Koide, Appl. Phys. Lett. **103**, 092905 (2013).
22. J. Liu, M. Liao, M. Imura, E. Watanabe, H. Oosato, and Y. Koide, Appl. Phys. Lett. **105**, 082110 (2014).
23. M. Zhang, W. Wang, G. Chen, H. N. Abbasi, Y. Wang, F. Lin, F. Wen, K. Wang, J. Zhang, R. Bu, and H. Wang, IEEE Tran. Electron Dev. **67**, 4784–4788 (2020).
24. Y. Kitabayashi, T. Kudo, H. Tsuboi, T. Yamada, D. Xu, M. Shibata, D. Matsumura, Y. Hayashi, M. Syamsul, M. Inaba, A. Hiraiwa, and H. Kawarada, IEEE Electron Dev. Lett. **38**, 363–366 (2017).
25. T. Bi, Y. Chang, W. Fei, M. Iwataki, A. Morishita, Y. Fu, N. Niikura, and H.

Kawarada, Carbon **175**, 525–533 (2021).

26. Y. Fu, Y. Chang, X. Zhu, R. Xu, Y. Xu, H. Kawarada. IEEE Tran. Electron Dev. **69**, 4144-4152 (2022).
27. T. Matsumoto, H. Kato, K. Oyama, T. Makino, M. Ogura, D. Takeuchi, T. Inokuma, N. Tokuda, and S. Yamasaki, Sci. Rep. **6**, 31585 (2016)
28. X. Zhang, T. Matsumoto, S. Yamasaki, C. E. Nebel, T. Inokuma, and N. Tokuda. J Mater Res. **36**, 4688–4702 (2021).
29. U. Choi, T. Kwak, S. Han, S. Kim, and O. Nam, Dia. Related Mater. **121**, 108782 (2022).
30. H. Umezawa, T. Matsumoto, and S. Shikata, IEEE Electron Dev. Lett. **35**, 1112-1114, (2014).
31. N. Saha, S. Kim, T. Oishi, and M. Kasu, IEEE Electron Dev. Lett. **43**, 1303–1306 (2022).

Figure captions

FIG. 1. (a) Depth profile of the SIMS measurement for concentration of boron atoms in the B-diamond epitaxial layer and (b) Cross-sectional high-resolution TEM image for the metal/Al_2O_3/B-diamond structure.

FIG. 2. (a) Scanning electron microscopy image and (b) schematic diagram of the B-diamond MOSFET, respectively.

FIG. 3. (a) and (b) I_D–V_D and I_D–V_{GS} characteristics for the B-diamond MOSFET, respectively.

FIG. 4. (a) $-\sqrt{|I_D|}$–V_{GS} characteristic for the B-diamond MOSFET. Inset figure shows schematic diagram for the formation mechanism of normally-off characteristic of the B-diamond MOSFET. (b) Breakdown voltage measurement for the B-diamond MOSFETs.

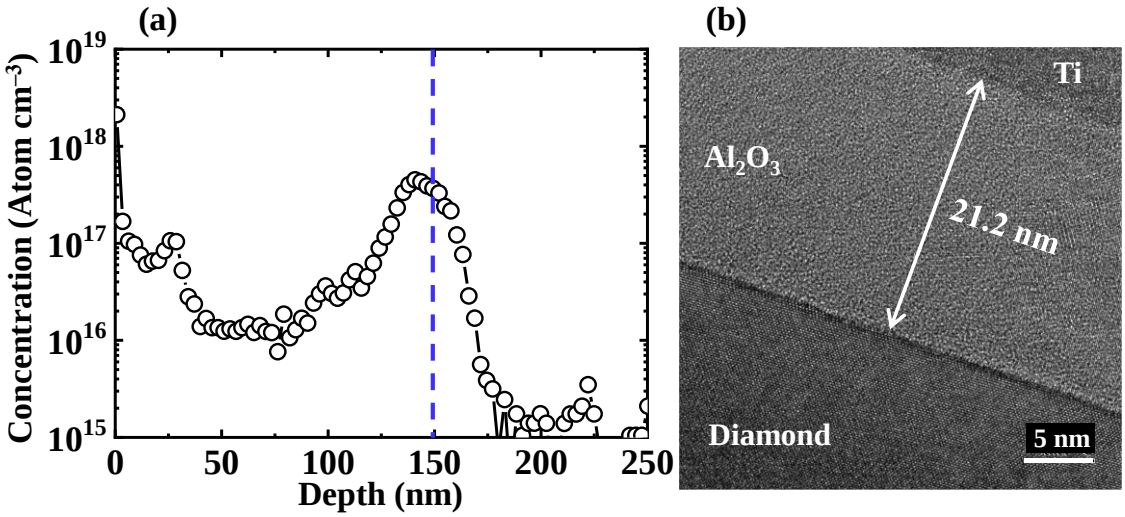

Liu *et al.*, Figure 1

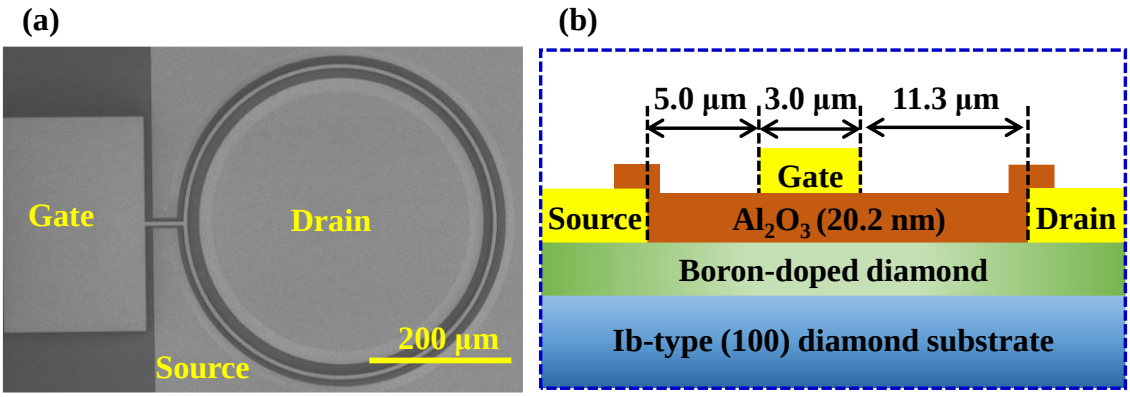

Liu *et al.*, Figure 2

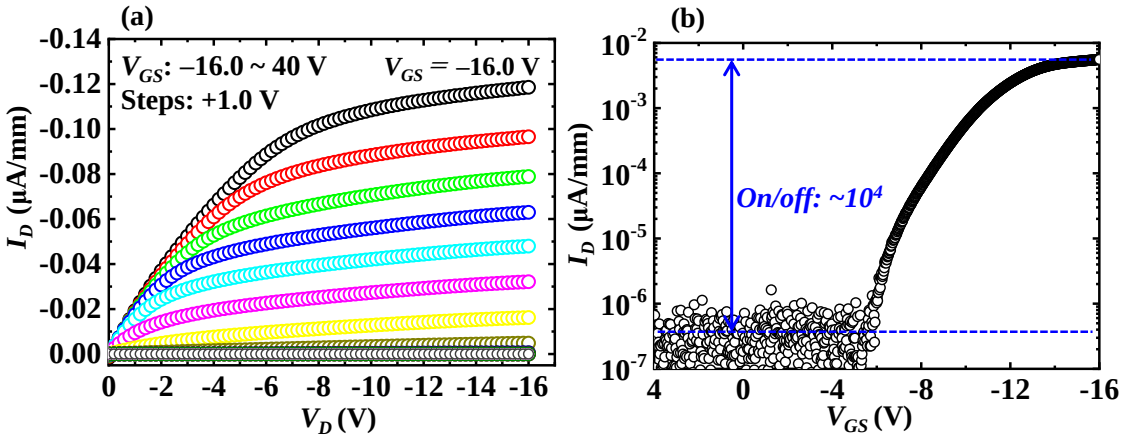

Liu *et al.*, Figure 3

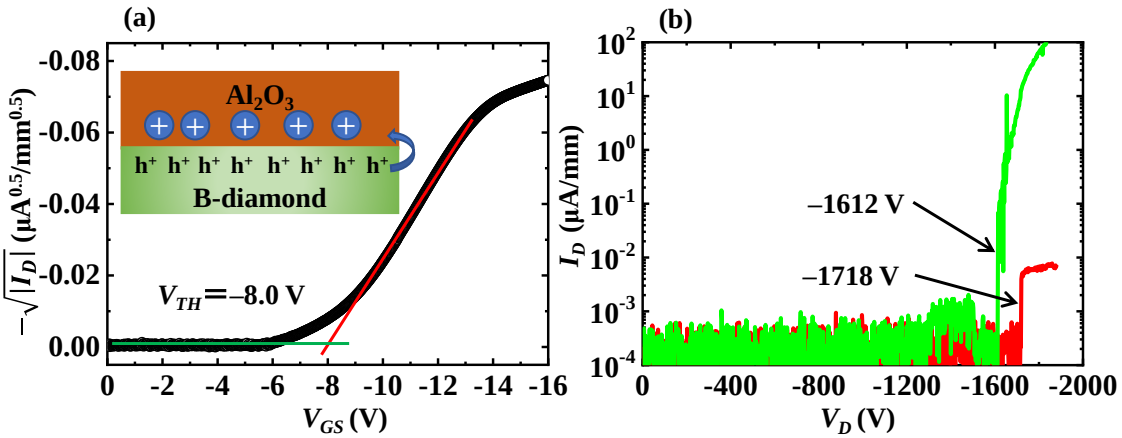

Liu *et al.*, Figure 4